NSF GRANT # 0529361
NSF PROGRAM NAME: Manufacturing Enterprise Systems

SIRG/Collaborative Research: Distributed Subwavelength Micro Photonic Sensors for In-situ Monitoring with High Spatial and Temporal Resolution in Manufacturing Environments

Xiaochun Li and Hongrui Jiang
University of Wisconsin-Madison

Brian Thomas
University of Illinois, Urbana-Champaign

David Dornfeld
University of California, Berkeley

Chee Wei Wong
Columbia University

Abstract: Micron-sized subwavelength structured photonic sensors could allow critical thermo-mechanical phenomena in manufacturing processes to be monitored, while offering tremendous advantages. To implement these novel sensors into real manufacturing processes, the microring sensors can be embedded at critical locations in metallic structures, which are heavily used in hostile manufacturing environments. This report presents our research activities on fabrication, embedding, and application of integrated mciroring sensors. For fundamental study, microring resonators have been microfabricated on-chip with silicon-on-insulator wafer substrates. The fabricated optical resonators offer Qs on the order of 20,000, enabling significantly improved temporal sensing and detection of high-frequency strain variation. A new approach to fabricate metal embedded photonic structures was developed. Various thin film photonic materials were studied for embedded microphotonic sensors. Effect of process parameters on refractive index of silicon nitride/silicon oxynitride films was studied. Metal embedded optical microring temperature sensors were characterized. The temperature sensitivity of the metal embedded microring sensor was 24.2 pm/oC. Issues on design and implementation of micro sensors for Chemical Mechanical Planarization (CMP) were studied. A design for the sensor and its installation into a continuous casting mold was also developed.

1. Introduction: Recent developments in integrated microphotonics have led to unprecedented potential towards robust sensor enhancements for manufacturing systems. These micron-sized subwavelength structured photonic sensors, e.g. microring and photonic crystal resonators, could allow critical thermo-mechanical phenomena in manufacturing processes to be monitored, while offering immunity to electromagnetic interference, resistance to hostile environments, multiplexing capabilities, and extremely high rates of data collection. Owing to their small sizes, distributed microphotonic sensors could be incorporated into mechanical structures without interfering with normal operation of the piece. The small size of these sensors enables them to respond to environmental changes (strain, thermal and vibrational) much more quickly than ordinary macro-sensors. In addition they permit data to be obtained with greatly enhanced spatial resolution and sensitivity.

Recent advances in photonic device microfabrication have made it possible to construct very small microring resonators in a variety of materials, including glass [1], polymers [2], silicon [3], silicon nitride (Si_3NH_4) [4], silicon oxynitride (SiON) [5], and III-V semiconductors [6]. The change in the resonant frequency $\Delta\lambda$ with respect to applied strain ε is related as: $\Delta\lambda/\lambda_o = n_{eff}\,[1 - \frac{1}{2}\,\wp(\varepsilon)\,n_{eff}^3]\,\varepsilon$, where λ_o is the resonant frequency, n_{eff} an effective refractive index, $\wp(\varepsilon)$ the photoelastic

coefficient as a function of strain. For strains on order 0.1%, the photoelastic correction term can be negligible, and the change in resonant frequency $\Delta\lambda$ is a linear function of strain ε. We also note here that $(\Delta\lambda/\lambda_o)$ is a linear function of temperature variations, and related as: $\Delta\lambda/\lambda_o = n_{eff}(\alpha+\beta)\Delta T/T$, where α is the linear thermal expansion coefficient and β the photothermal coefficient expressing dependence of refractive index on temperature. For a given signal-to-noise limit in tracking motion of a Lorentzian peak, therefore, the strain sensitivity of microring resonators to external strain perturbation is identified by Q $(=\lambda_o/\delta\lambda)$. For example, if one conservatively assumes a 3-dB differentiation limit between two overlapping Lorentzian peaks, the resolution in strain detection is proportional to $\delta\lambda$ or equivalent to λ_o/Q. Combining with $\Delta\lambda/\lambda_o = n_{eff}[1 - \frac{1}{2}\wp(\varepsilon) n_{eff}^3]\varepsilon$, this gives a strain resolution as proportional to 1/Q: that is, a larger Q gives a better strain resolution. Microring resonators, in high-index contrast silicon material systems, have reported Q on order 8,000, and up to even 57,000 [7].

To implement these novel sensors into real manufacturing processes, the microring sensors must survive hostile environments and provide high accuracy, long-term stability, and good reliability during service. To achieve this goal, distributed microring sensors can be embedded---thus avoiding direct exposure from external manufacturing environments (e.g. chemicals, moisture, contamination etc.)---at critical locations but without interfering with normal operation of the structure. The small size of these sensors will permit data to be obtained with significantly enhanced spatial and temporal resolution as well as superior sensitivity. Challenges for microring sensor embedding arise from the fact that most structures used in hostile manufacturing environments are metallic. It is necessary to fabricate and embed microphotonic sensors into metal wafers before the sensors can be implemented. SiO2-based Fiber Bragg Grating (FBG) sensors have been successfully embedded into nickel and stainless steel for temperature and strain measurements in laser-based manufacturing [8-12]. Moreover, micro optical thin films are expected to demonstrate much superior properties than their macro optic counterparts, e.g. amorphous micro/nano SiO2 and Si3N4 thin films actually have significantly higher strain limit (3~10%) than that of most metals (0.2~1%) [13]. Thus, it is promising to fabricate metal embedded microphotonic sensors that can withstand the hostile manufacturing environments.

The successful implementation of these embedded microphotonic sensor arrays could advance the fundamental understanding of manufacturing processes, thus significantly improving productivity and generating significant cost savings. To date, a systematic study of these subwavelength microphotonic sensors for strain and temperature measurements has yet to be conducted that would allow the potential of these devices to be fully harnessed for manufacturing processes. This paper presents our research progress on integrated subwavelength photonic sensors that offers exciting new opportunities for fundamental understanding and better control of manufacturing processes.

2. Detailed Analysis on Microring Sensor Principle: Ring resonators are widely used in optical communication as wavelength-division multiplexing (WDM) add/drop filters. A ring resonator system may be composed of one or two bus waveguides and a ring placed very close to them. When a light beam with a range of wavelengths is shot into the straight waveguide, the light with resonant wavelength will resonate in the ring cavity, which can further be coupled to another straight waveguide, as shown in Fig. 1.

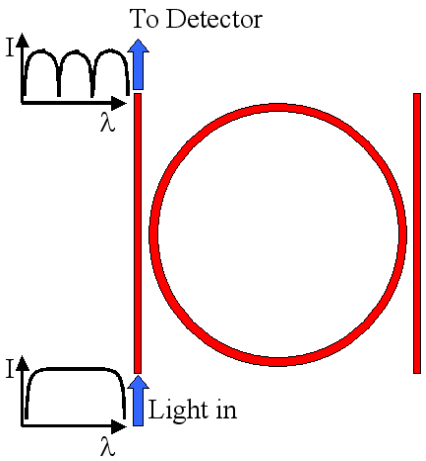

Fig. 1 Transmission spectrum of an optical waveguide coupled to a ring resonator

The resonant wavelength of a microring resonator can be expressed as:

$$\lambda_o = \frac{2\pi R n_{eff}}{m} \quad (1)$$

Where R is the radius of the ring, n_{eff} is the effective refractive index of the ring and m is an integer. When thermal loads are applied to the ring, due to photothermal effects and thermal expansion, n_{eff} and R will change so that the resonant wavelengths (i.e. the dropped ones in Fig. 1 after

passing through the ring resonator) will also change. By tracking the wavelength shifts, temperatures can be measured.

By differentiating Eq. (1), the resonant wavelength shift $\Delta\lambda$ is given by:

$$\Delta\lambda = \frac{2\pi}{m}\left(n_{eff}\Delta R + R\Delta n_{eff}\right) \quad (2)$$

Thus, the temperature dependence of resonant wavelength shift is related to the changes of effective refractive index and thermal expansion through the equation:

$$\frac{\Delta\lambda}{\lambda} = \left[\alpha + \frac{1}{n_{eff}}\left(\frac{dn}{dT}\right)\right]\Delta T \quad (3)$$

Where α is the effective coefficient of linear thermal expansion of the sensor material, and dn/dT is the photothermal coefficient expressing dependence of the effective refractive index on temperature. For a given signal-to-noise limit in tracking motion of a Lorentzian peak, therefore, the resolution of microring sensors to external temperature perturbation is identified by Q ($=\lambda_o/\delta\lambda$), the ratio of the resonator operating wavelength λ_o to the resonator full-width half-maximum (FWHM) $\delta\lambda$. For example, if one assumes a 3-dB differentiation limit between two overlapping Lorentzian peaks, the resolution in temperature detection is proportional to $\delta\lambda$ or equivalent to λ_o/Q. Combining with the relation between $\Delta\lambda$ and temperature, as shown in Eq. (2), this gives a temperature resolution proportional to 1/Q, that is, a larger Q gives a better temperature resolution. For microring resonators, Q from 400 in low-index contrast material systems up to even 57,000 in high-index contrast silicon material systems has been reported.

3. Fundamental Study on Microring Resonators for High Spatial and Temporal Resolution Strain Sensors: Microring resonators have been microfabricated on-chip with silicon-on-insulator wafer substrates (hence permitting CMOS-level batch processing) and each chip packaged to signal (input) and detector single-mode optical fibers.

In the development of high-performance microphotonic sensors, the traveling wave microring resonator (on order several micrometers) is one of the critical elements towards high strain sensitivity, high spatial resolution and short temporal resolution. The strain sensitivity is dependent on the spectral linewidth of the microphotonic resonator – our focus is to develop high-quality factor optical resonators and with oxide, nitride, oxynitride material systems for embedding in metals to enhance sensor reliability (see Fig. 2). In addition, we investigate numerically the optical coupling efficiency from designed gratings into the optical waveguides.

Microring resonators (such as studied in our group, as shown in Fig. 2) are traveling wave resonators with the transmission response following a Lorentzian line shape filter. The microring becomes a resonant sink for the signal power when an integral number of wavelengths match its optical circumference. A characteristic of microring resonators is the quality factor *Q*: a measure of its extrinsic and intrinsic losses, a measure of its detection sensitivity for localized strain (thermal or mechanical) sensing, and a measure of the ultimate response time (continuous strain event monitoring) of these sensors. *Q* is defined as $\lambda_0/\delta\lambda$, the ratio of the resonator operating wavelength λ_o to the resonator full-width half-maximum (FWHM) $\delta\lambda$. The resonance will be tracked to determine the external strain on the microring sensors. The resonant spectral modes are illustrated in Fig. 3, through the discrete Fourier transform of a temporal pulse in the resonator. The numerical simulations (a few to several hours on cluster or stand-along machines) are performed in RSoft FullWave, a finite-difference time-domain solver of Maxwell's equations.

Recent developments on optical resonators in our group have experimentally measured loaded *Q*s on order 20,000 – two to three orders of magnitude better than conventional fiber Bragg sensors. This is illustrated in Fig. 4. Using optical fiber input and output coupling to the resonators, speed of light data transmission is obtained between the individual sensors and the data collection endpoints in the sensor network. This permits significantly improved temporal sensing and detection of high-frequency strain variation, supported even with commercial off-the-shelf photodetectors through wavelength-division multiplexing. The small-sized resonators also permit spatial resolution at least two orders of magnitude better than conventional fiber Bragg sensors.

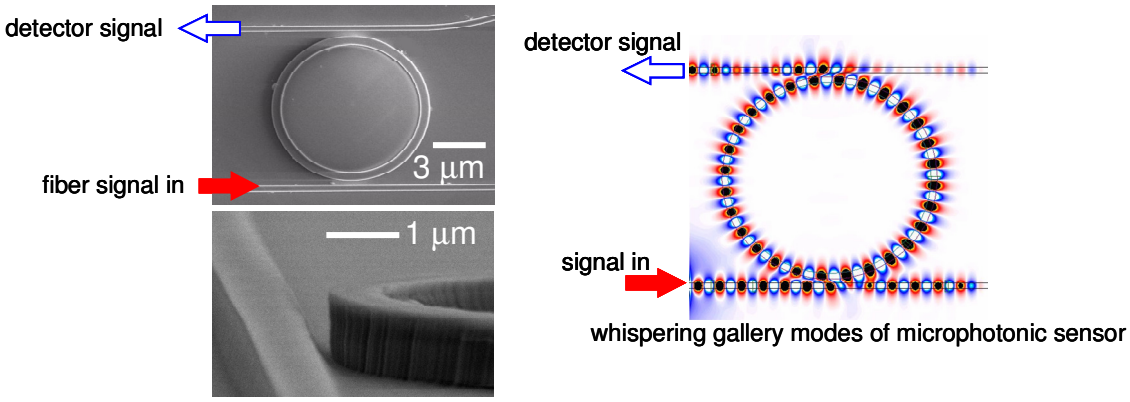

Figure 2. Microring optical sensors fabricated through the Columbia – Wisconsin Madison collaboration

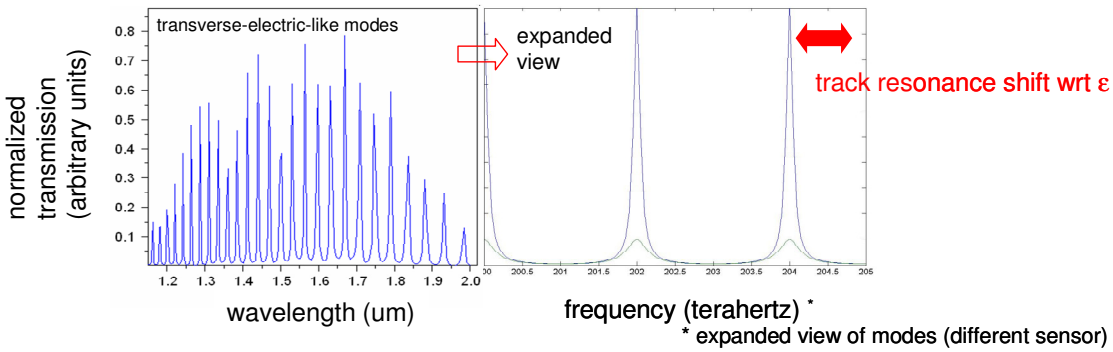

Figure 3. Numerical spectral of microring resonators

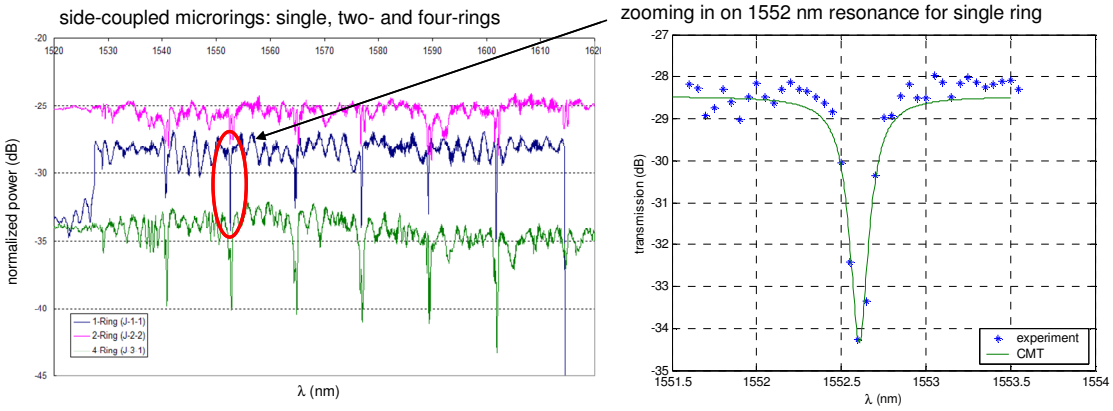

Figure 4. Experimentally measured resonances of microring sensors
Left panel: spectrum of resonators for 1,2 and 4 rings
Right panel: expanded view of measurement data with CMT theory comparison

4. Study on embedding of microring sensors in metals

4.1. Material Selection and Sensor Design:

4.1.1 Material Selection: Generally, a passive photonic device consists of two types of photonic materials with a certain reflective index (n) contrast. The lower n material is used as cladding, and the one with higher n is used as the core for guiding light.

In this study silicon dioxide, which is widely used as a cladding material for optical fibers, was selected to serve as the cladding material for our ring resonators. Silicon nitride/silicon oxynitride was selected as the core material. It should be noted that the reflective index of silicon nitride/ silicon oxynitride deposited by Plasma enhanced chemical vapor deposition (PECVD) could be tuned by using different gas flow rates and different gas mixtures. With various process conditions, as listed in Table 1, the refractive index varies from pure silicon dioxide to silicon-rich silicon nitride, as shown in Fig. 5.

Table 1 PECVD Process Conditions

Material	SiH_4	NH_3	N_2	NO_2
1.Si_xN_y	10sccm	4sccm	1000sccm	-
2.Si_xN_y	8sccm	4sccm	1000sccm	-
3.SiO_xN_y	10sccm	4sccm	-	800sccm
4.SiO_2	8.8sccm	-	-	1200sccm

Base pressure: 0.5mTorr. Deposition temperature: 300°C. Power: 50W

Table 2 Sellmeier coefficients for Si_xN_y and SiO_2

Material	B_1	B_2	B_3	C_1	C_2	C_3
Si_xN_y	1.0905	1.1179	0.5921	6.1683×10^5	6.1683×10^5	-3.1077×10^5
SiO_2	0.3813	0.3841	0.2768	2.9331×10^4	2.9331×10^4	-5.5520×10^4

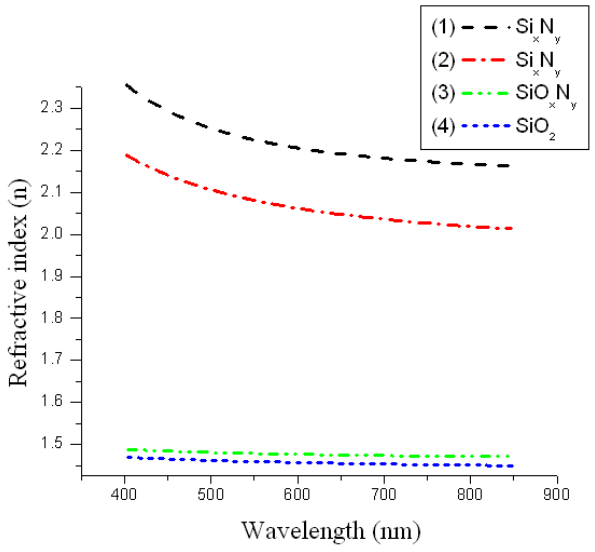

Figure 5. Refractive index varied with various wavelengths and process conditions

Filmetrics F-20 optical reflectometer was used to measure refractive indices of the silicon dioxide and silicon nitride films. However, it can only measure the refractive indices at the wavelength range from 400 nm up to 850 nm. Since the sensor working wavelength was designed in the infrared (IR) range, Sellmeier equation, which is an empirical relationship between refractive index and wavelength for transparent medium, was applied to estimate the refractive index in the IR range. The form of the third order Sellmeier equation is:

$$n^2(\lambda) = 1 + \frac{B_1\lambda^2}{\lambda^2 - C_1} + \frac{B_2\lambda^2}{\lambda^2 - C_2} + \frac{B_3\lambda^2}{\lambda^2 - C_3} \quad (4)$$

Where $B_{1,2,3}$ and $C_{1,2,3}$ are experimentally determined Sellmeier coefficients. Based on the measured data points, Sellmeier coefficients for Si rich Si_xN_y and SiO_2, the materials for sensor fabrication, were derived and listed in Table 2. According to Eq. (4) and the coefficients, refractive

indices of Si_xN_y and SiO_2 in the IR range can be estimated.

Nickel was selected as the substrate material due to its capability to function well in hostile environments. It has a high melting point, up to 1455 ºC, and a good corrosion resistance to acids, alkalis and oxidizing agents. Furthermore, nickel offers good mechanical properties, especially good ductility. It can be easily deposited by electroplating at a high rate at room temperature.

4.1.2 Sensor Design: The metal embedded waveguide structure is illustrated in Fig. 6. The basic limitation to the resonator, and therefore to the waveguide design, was the need to propagate light in a small radius of curvature with a minimum loss, and to ensure a single mode propagation. Therefore the thickness of top and bottom SiO_2 was chosen as 3 µm to minimize the light loss. The height of the core (Si_xN_y) was designed as 0.5 µm, so that the light could be vertically confined in the waveguide well.

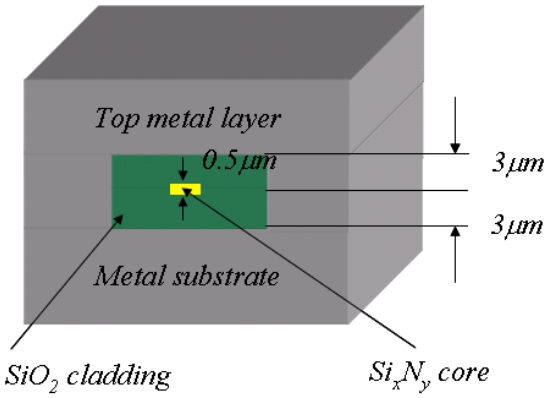

Figure 6. Metal embedded photonic waveguide

To decide the width of the waveguide core, RSoft – FullWave (a finite-difference time-domain solver of Maxwell's equations) was applied for waveguide simulation. As shown in Fig. 7, the waveguide behaves in single mode with little leakage to the top and bottom metals when the width of the waveguide core is 1 µm, and thus, light is very well confined in the core area.

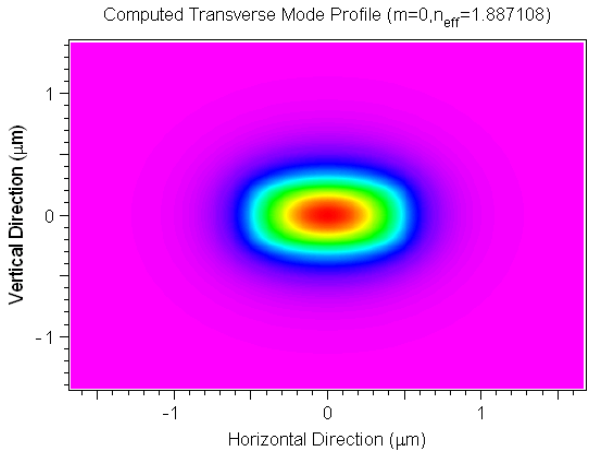

Figure 7. Simulation of waveguide

Since the waveguide size was only 1 µm, a taper was introduced to facilitate a later input optical fiber alignment and increase the alignment tolerance. The wider waveguide size was designed to be 10 µm, and its taper length was determined by a parametric study using RSoft – FullWave. The length of the taper was scanned from 10 µm to 100 µm, and finally was set as 45 µm, at which the loss was around 10% only, as shown in Fig. 8.

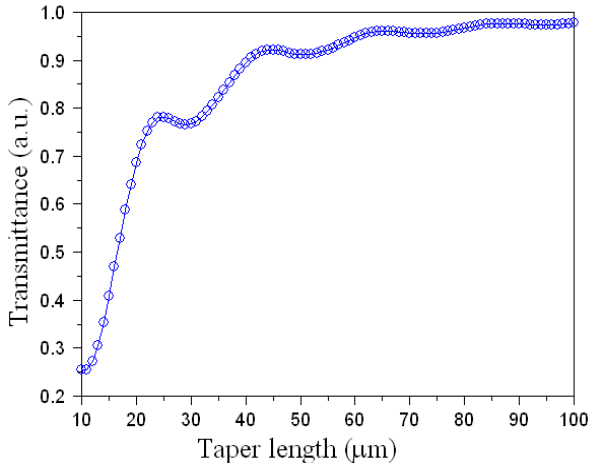

Fig. 8. Parametric study of taper length

To minimize the bending loss of the ring, a model based on effective index method was employed to design the ring radius. Figure 9 illustrates the simulation results. A radius of 30 µm was chosen to guarantee minimal bending loss.

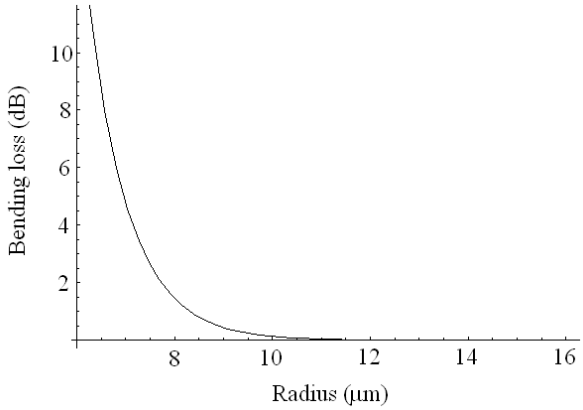

Fig. 9. Simulation of bending loss

A 200nm coupling gap was used so that light can be coupled between the straight waveguide and the ring more efficiently. Figure 10 demonstrates the layout of a microring sensor.

4.2. Sensor Fabrication: In this study, based on standard microfabrication and electroplating techniques, a batch of microring sensors was fabricated on an electroplated metal wafer and then embedded. Details of the fabrication are depicted in Fig. 11 and will be described below.

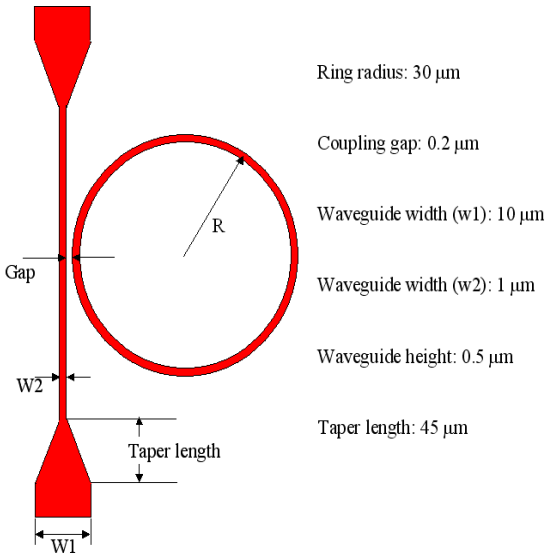

Fig. 10 Dimensions for ring resonators

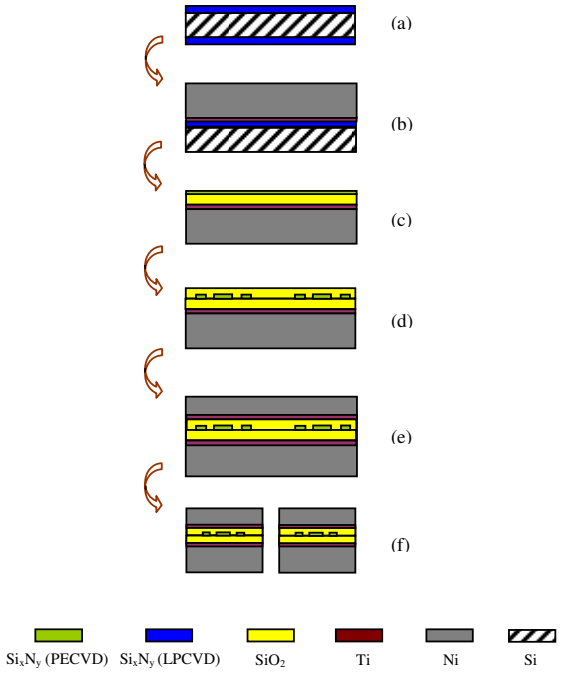

Fig. 11. Sensor fabrication process flow
a) Deposit Si_xN_y by LPCVD on Si, b) Sputter Ti/Ni followed by Ni electroplating then etch out the backside Si_xN_y, c) Deposit SiO_2 and Si_xN_y by PECVD on metal wafer, d) Employ hybrid lithography and RIE to define sensor structures, deposit top SiO_2 by PECVD, e) Sputter Ti/Ni and electroplate Ni again to embed sensors f) Dicing sensors into single units

A 3-inch silicon wafer was first thoroughly cleaned by pre-furnace cleaning. Then a thin layer of low stress silicon nitride (0.5 μm thick) was deposited by low-pressure chemical vapor deposition (LPCVD) to serve as an etch stop layer for the subsequent KOH etching of the silicon wafer. A thin layer of Ti (50 nm) was then sputtered as an adhesion-promoting layer, followed by a Ni seed layer (300 nm). The structure was then electroplated to create a nickel substrate (approximately 220 μm) on one side. After electro-deposition of Ni, the silicon nitride (deposited by LPCVD) on the backside of the silicon wafer was etched out by reactive ion etching (RIE), and the silicon wafer was completely etched out in a 30% KOH solution at 80 ºC. The other silicon nitride layer was removed by RIE to form the metal wafer.

On the top surface of the metal wafer, a 3 μm thick silicon dioxide layer followed by a 0.5 μm thick silicon nitride layer were deposited by PECVD. Figure 11(c) shows the structure at this stage.

Since the gap between the waveguide core and coupling is only 200nm wide, electron beam (e-

beam) lithography was used for patterning. Hence a hybrid lithography technique (i.e. photo/e-beam lithography combination) was applied for the sensor fabrication. S1813 with LOR 3A was patterned by optical lithography for lift-off. Thin films of Cr/Au (5/50 nm) were evaporated and followed by lift-off process to obtain etching mask and alignment marks for the e-beam lithography. Co-polymer (MMA) and PMMA bi-layers were spin coated, followed by e-beam lithography, and then Cr/Au thin films were evaporated on the top again. After lift-off, RIE with CF_4 plasma was used to etch the silicon nitride. Figure 12 is the scanning electron microscopy (SEM) image of the fabricated microring at this step. Upon the complete removal of Cr/Au films, a 3 μm thick silicon dioxide layer was again deposited by PECVD to clad the waveguide core. Figure 11(d) indicates the sensors on a metal wafer.

To embed these microring sensors into nickel, more fabrication steps were needed. Ti/Ni layers were again sputtered, and a thick nickel layer (e.g. around 70μm in this study) was electroplated to embed sensors. Figure 11(e) shows the Ni embedded optical sensors. Each single metal embedded sensor unit can be further diced out from the metal wafer using laser cutting or diamond saw dicing.

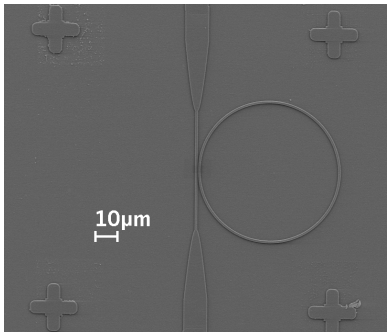

Fig. 12. SEM image of optical microring

4.3. Experiments and Results: To investigate the functionality of the metal embedded photonic structures, metal embedded optical waveguides, which are the basic elements of the optical sensors, were first tested. Figure 13 shows the waveguides before and after embedding. The embedded structures were mounted in epoxy followed by polishing ended with colloidal silica (50 nm). Figure 14 illustrates the polished facet of metal embedded waveguides, and the pattern of the output light.

After fabrication of sensors on metal substrate, they were selectively electroplated to embed the sensing part (microrings), so that the waveguide can be exposed for a better light coupling. Focused ion beam (FIB) was used to polish the sensor facets for light coupling and to mill a slot for fiber insertion. Figure 15 shows an example of FIB machined sensor and its polished facet.

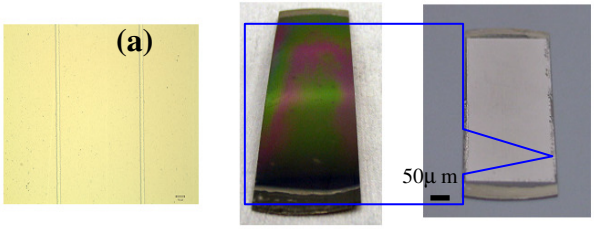

Fig. 13 (a) Waveguides before embedding, (b) Metal embedded waveguides

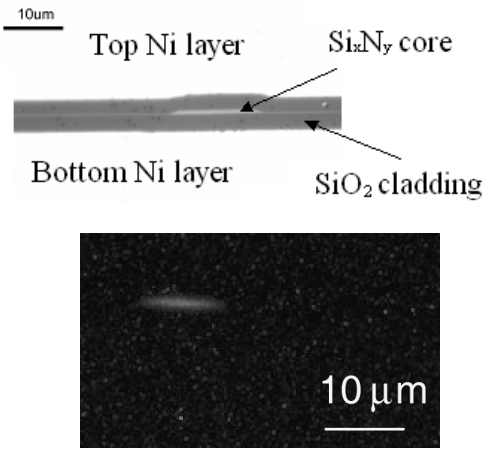

Fig. 14 (top) Polished embedded waveguide facet, (bottom) Output light pattern

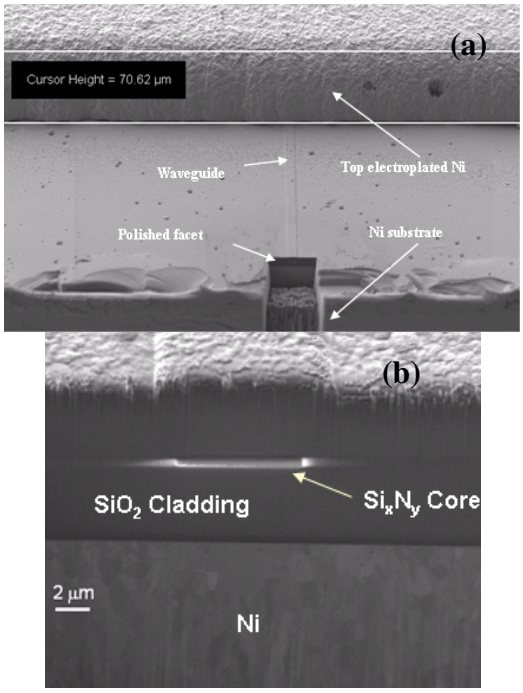

Fig. 15 (a) FIB machined embedded sensor, (b) Polished waveguide facet

The characterization was conducted using the experimental setup illustrated in Fig. 16. The FIB machined sample was fixed on a micro-stage. Tapered pigtailed fibers with a tip diameter of 2 μm were obtained by HF etching [17]. The tapered fibers were attached on the micro-stage by fiber holders. An AHURA Corporation superluminescent LED (SPOA-B35-1410-100-B14) was used as the input light source. The output light was collected by a tapered fiber tip and connected to an Agilent 86142B optical spectrum analyzer (OSA). A soldering iron tip was placed near to the sample to serve as a tunable heat source and two K-type wire thermocouples were attached near to the ring to provide the actual temperature.

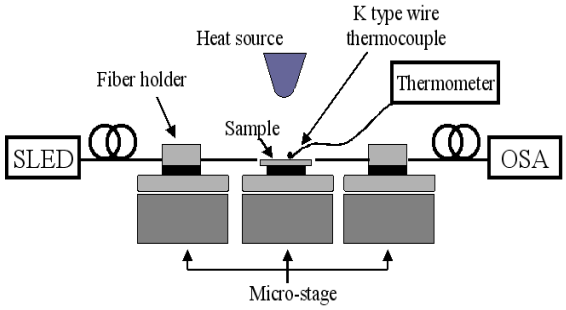

Fig. 16. Experimental setup for characterization

Figure 17 shows the measured spectral response (normalized to its maximum) for the microring resonator at room temperature (25.5 ^{o}C). The measurements indicate the Q factor of the resonator is around 2000, and FSR is about 5.2 nm. It should be note that the fluctuation in transmittance could be introduced by the misalignment caused by fiber vibration.

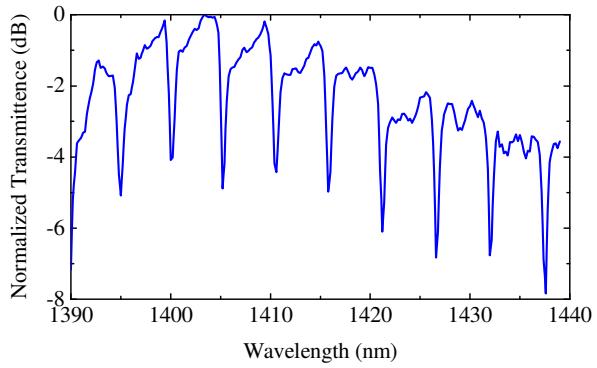

Fig. 17. Measured spectral response (normalized to maximum) at room temperature

Resonant wavelength shift with temperature is shown in Fig. 18. Lorentz fitting was employed to determine the shift in resonance. As the temperature rose from 25.5^{o}C to 88^{o}C, the resonant peak shifts from 1405.29nm to 1406.81nm. Figure 19 illustrates the relationship between resonant wavelength and temperature. The linear fitting equation shows the temperature sensitivity of the device is 24.2 pm/^{o}C.

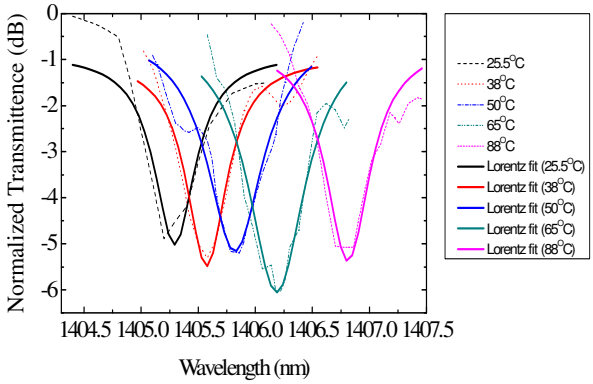

Fig. 18. Spectral response (normalized to maximum) with respect to temperature

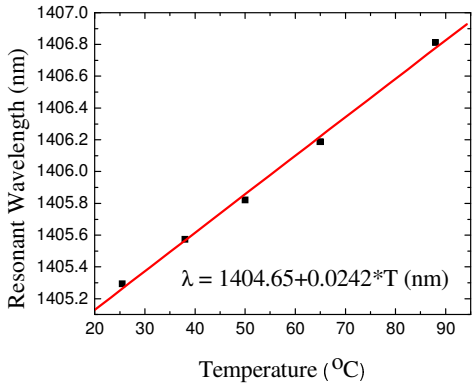

Fig. 19. Resonant wavelength as a function of temperature

Theoretical temperature sensitivity can be estimated by Eq. (3). With the assumptions of a constant coefficient of thermal expansion (CTE) for nickel, and a perfect bonding between the optical thin films and electroplated nickel, the temperature sensitivity was calculated to be 23.6 pm/^{o}C. The theoretical sensitivity was about 3% smaller than that from experiments. The difference might be attributed to errors in the estimated refractive index n_{eff}, 1.887, the constant CTE of nickel, 12 με/^{o}C, and dn_{eff}/dT, $9.1*10^{-6}$/^{o}C. It is especially difficult to obtain an accurate value of dn_{eff}/dT (since it is a processing dependent value) and the CTE mismatch between silica and silicon nitride could also introduce some errors on dn_{eff}/dT.

5. Research Progress on Implementation of Sensors for Manufacturing Processes: Two important manufacturing processes, Chemical Mechanical Planarization (CMP) [14,15] and Continuous Casting of steel [16], will be used as

testbeds to test the novel high spatial, temporal and sensitivity resolution sensor in demanding manufacturing environments.

5.1. Analysis for design and implementation of sensors for CMP: The integration of sensors in CMP will allow the progress of fundamental study and model development. In addition, sensors will enable real time manufacturing feedback for improved process monitoring and control. Despite the acceptance of CMP in IC manufacturing, there is little known of the CMP interface at the micro scale. The only sensors currently used in CMP are on the macro or machine scale. As seen in Table 3, machine level sensors are most prominently used for end point detection via optical sensors and motor current sensors. Pad and wafer embedded sensors allow for the characterization of many more aspects of the CMP process.

To reach the micro scale, sensors must be placed closer to the interface. There are two options, embedding sensors on the wafer or embedding sensors on the pad. Wafers can be embedded with micro contact pressure sensors. Alternatively, sensors can be embedded into the pad. Both pad and wafer sensors have their own advantages.

Sensors in the wafer allow the highest resolution and will most accurately reflect interactions on the interface. However, since CMP is a destructive process, the wafer sensors will become miscalibrated after only a short time elapse and will eventually be destroyed completely. It would also be unlikely for sensors to be embedded on a production wafer which is to be used in an actual manufacturing process. Thus, sensors on wafers can only be used for fundamental study and model development in laboratory settings.

Table 3: Uses of sensors in the Pad, Wafer, and Machine

Sensor location used for	PAD	WAFER	Machine
In-situ monitoring of wafer to wafer pad degradation	**Thin Films, MEMS resonator**		**Acoustic Emission**
Monitoring spatial variation of pad degradation	**Thin Films, MEMS resonator**		**Acoustic Emission**
In-situ feed back control of head zone pressure	**Thin Films, MEMS resonator**		
Ex-situ head zone pressure optimization	**Thin Films, MEMS resonator**	**MEMS capacitance**	
In-situ scratch detection			**Acoustic Emission**
End point detection			**Motor current, Acoustic Emission** **Optical**
Ex-situ pattern effect characterization		**MEMS capacitance**	
Modeling parameter extraction & fundamental study	**Thin Films, MEMS resonator**	**MEMS capacitance**	

direct

indirect

Sensors in the pad allow for real time manufacturing monitoring and control. Within Wafer Non Uniformity (WIWNU) is a large issue in fabrication facilities. It is compensated with carrier head back pressure zone variation; however, current monitoring of WIWNU effects are measured ex situ. This lack of real time control loop not only slows the production process, it can decrease yields substantially. Pads embedded with sensors would allow for in situ real time control for optimal zone back pressure.

In addition to WIWNU detection, a sensor embedded pad could detect pad degradation and variation of pad degradation. The largest drawback of a pad embedded sensor is that asperity level resolution would not be possible. As seen in Figure 20, spatial resolution is a function of local sensor

resolution and distance from surface. The exact sensitivity must be determined experimentally since pad material properties vary from pad to pad.

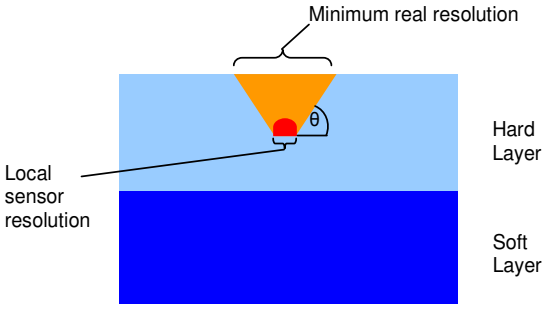

Figure 20. Schematic of an embedded sensor and effects of location on spatial resolution

Non destructive removal of pad sections has proven difficult. Thus, to remove the soft layer, we propose to remove the material on a mill. As seen in Figure 21, we can machine a 3 inch diameter blind hole into the back of the pad. With this method, we can customize the precise depth of the hole. The 3 inch sensor array will be imbedded directly onto the backside of the hard layer. In our lab, we have access to 30 inch pads which are oversized for our GNP CMP machine. We can graft a 3 inch diameter section from the unused portion of the pad and use it as the soft layer. The grafting from the same pad is necessary due to inconsistencies in material from pad to pad. Subtleties such as storage humidity or date of manufacture can alter pad hardness modulus.

The actual grafting process can be seen in Figure 22. The cross section is show in 3 steps: machining the soft layer, machining the hard layer, and grafting the two together with the sensor at the interface. With this process, the depth of sensor in the pad can be chosen. For example, the sensor can be half way into the hard layer or just at the interface.

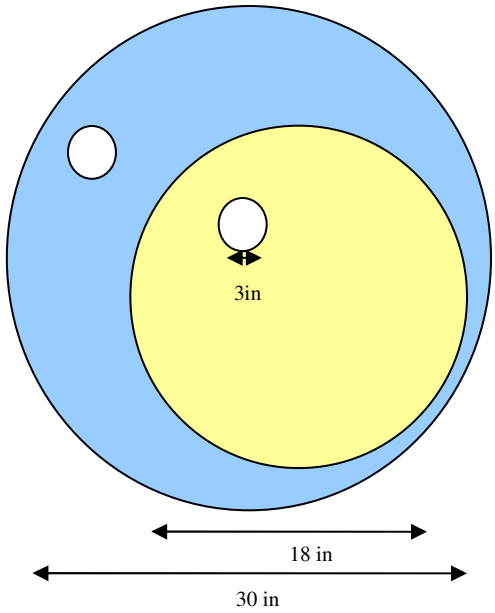

Figure 21. The blue colored circle represents a commercially available 30 inch pad. The yellow colored circle represents the 18 inch diameter pad necessary for the GNP machine at UC Berkeley. The white circles represent the machined sensor location and the grafted section.

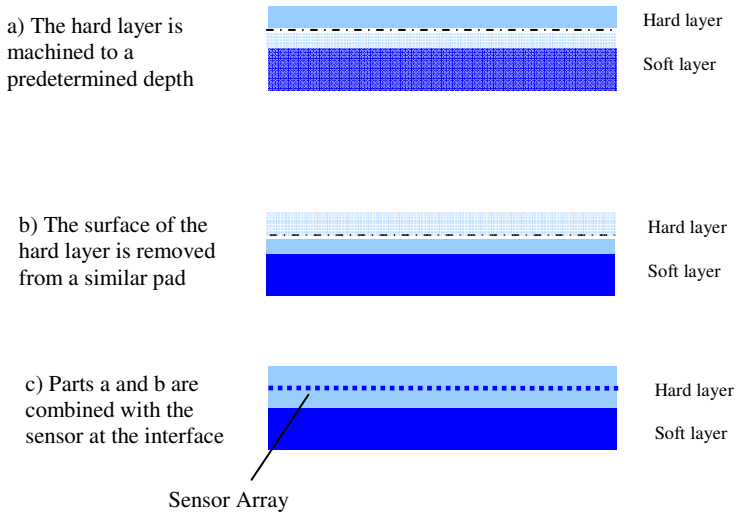

Figure 22: Grafting process cross section. As shown, the sensor is half way into the hard layer.

5.2. Design of an In-situ Pressure/Shear Monitoring System for CMP: Chemical Mechanical Polishing—a key process in semiconductor manufacturing—could benefit significantly from in-situ pressure and shear feedback. Currently, there is no mechanism for measuring the distribution of said loads across the surface of the wafer while it is being polished. This paper evaluates a proposed sensor designed for placement beneath the CMP pad. Various challenges arise from the fact that the sensor is to be installed on a rotating surface. A wireless data-acquisition-system has been developed to overcome this complication, and is also presented in the paper.

There are various options for measuring pressure fields. Pressure sensor arrays, such as Tekscan's *I-Scan* or SPI's *Tactilus* include CMP among their target applications. Examples of graphic output from these two sensors is presented , Figures 23 and 24. While the sensors do provide dynamic, real-time measurements, they are not suitable for use under shear (i.e. while the wafer and/or pad are rotating or translating), significantly limiting their usefulness for this application.

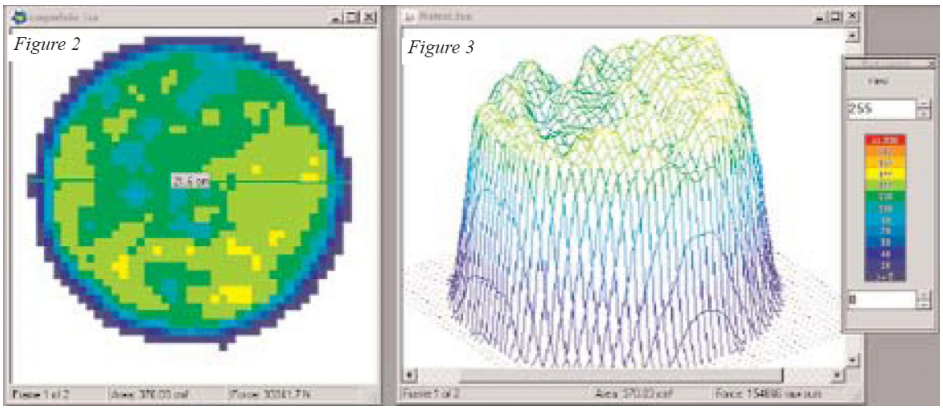

Figure 23 Tekscan CMP image

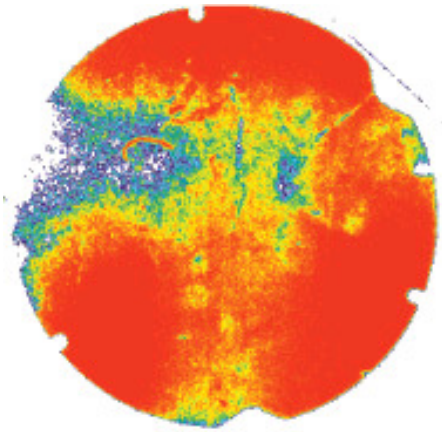

Figure 24. Tactilus CMP image

An alternate approach to integrating sensors in or beneath the pad is to integrate sensors in the wafer. Wafer-embedded sensors have the benefit of providing direct measurements with high spatial sensitivity. In-situ monitoring of actual production devices would require every wafer to be equipped with sensors, limiting the number of devices that can be put on a given wafer, and requiring all existing wafer layouts (photo-lithography masks, etc.) to be redesigned. This proposition would likely be met by resistance from industry, and thus primarily holds promise for research applications.

Modern CMP systems are not entirely without feedback control. While there is no way to measure the pressure distribution during processing, there are methods in place for measuring the MRR directly. These include optical techniques such as laser interferometry—useful for measuring film thickness—and eddy-current sensing for detecting copper thickness. Although useful for end-point detection (determining when polishing is complete), these techniques are not feasible for achieving full-field measurements.

Within industry, there is also an interest in the measurement of shear forces applied to the wafer. On the macroscopic scale, shear force (frictional force) and pressure are proportional. However, in the case where the pad asperity size is of the same order of magnitude (or smaller) as feature size, local shear forces are not always a function of pressure. Since there may be some degree pattern dependency on the local shear forces, it may be beneficial to provide measurements shear forces across the wafer surface.

5.2.1. Effects of Pad Properties: As discussed, the placement of sensors beneath the polishing pad is preferred for economic reasons but results in a loss of accuracy. This section evaluates the effects of a polishing pad on data recorded by sub-pad sensors. More specifically, it is determined how the pad properties and thickness affect the minimum area over which a pressure must be applied to yield 96% transmission of the pressure to the base of the pad.

There are a variety of pads used for CMP, each with their own performance benefits. Hard, stiff pads are used to achieve good local planarity, while softer pads provide better global planarity. Typically a stacked configuration is used, consisting of a hard top-pad and softer base-pad, combining the benefits of both pad types. CMP pads are generally polymer based, but can be manufactured to have different microstructures, yielding varied mechanical properties and surface topology, and consequently, varied polishing performance.

The mechanical properties of the various pads are generally poorly documented. Furthermore, the values in literature for a given pad were found to vary significantly. The best documented pad type is the Rohm and Haas IC1000, likely due to it's prevalence within industry. The IC1000 is closed-cell polyurethane foam with high stiffness. It exhibits a Young's Modulus of ~310MPa and a thickness of 2.54mm. Throughout the literature, a value of 0.1 was assumed for Poisson's ratio. As discussed, using a softer pad beneath a hard pad such as the IC1000 provides improved global planarity. A typical combination is the IC1000 with a SUBA IV sub-pad (assume E=31MPa, ν=0.1), both layers 1.397mm thick. The cross-sectional image of an IC1000 pad with SUBA IV sub-pad is shown in Figure 25.

Figure 25. IC1000/SUBA IV cross-section

The pad exhibits some degree of viscoelastic behavior (i.e $\tan(\delta)=0.090$), leading to gradual changes in the pad thickness and apparent stiffness of the pad during polishing[Error! Reference source not found.]. The phase shift and dynamic effects due to transmission through a viscoelastic pad should have negligible effects on sub-pad sensor measurements since the frequency of the applied loads are relatively low.

5.2.2. Pressure Decay: To model the influence of the pad properties on pressure transmission, ABAQUS finite element analysis software has been used. For computational simplicity, an axisymmetric model was generated, shown in Figure 26. The model was meshed with CAX4R quad-type elements and a 5 psi load with radius *r* was applied at the center of the circular model. The adhesion between the pad and platen is ignored for modeling purposes.

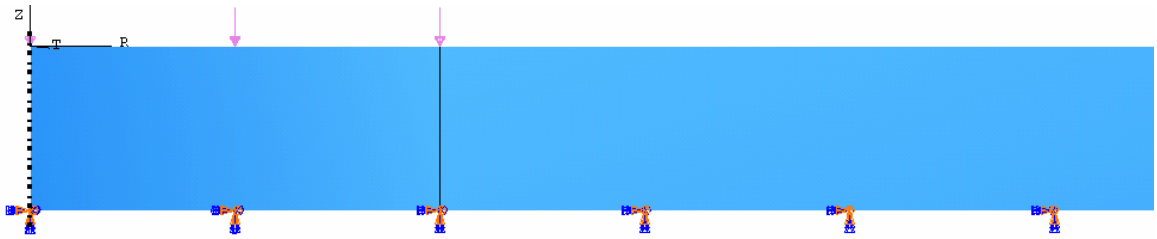

Figure 26. Axi-symmetric pad model (ABAQUS)

Figure 27a/b illustrates the force attenuation that is being characterized. When *r* is sufficiently large, the full magnitude of the force can be sensed at the base of the pad at the center of the load, as shown in Figure 27a. However, loads with very small radii can not be detected at the base of the pad, as Figure 27b illustrates.

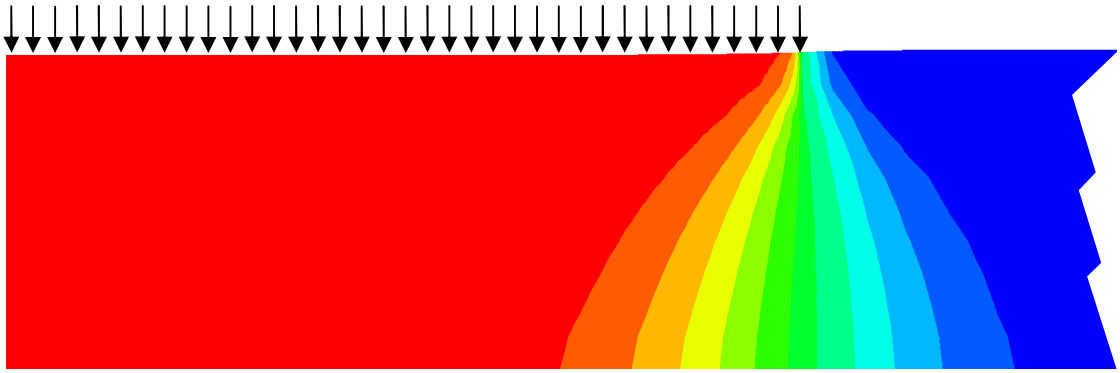

Figure 27a. Force attenuation for large load

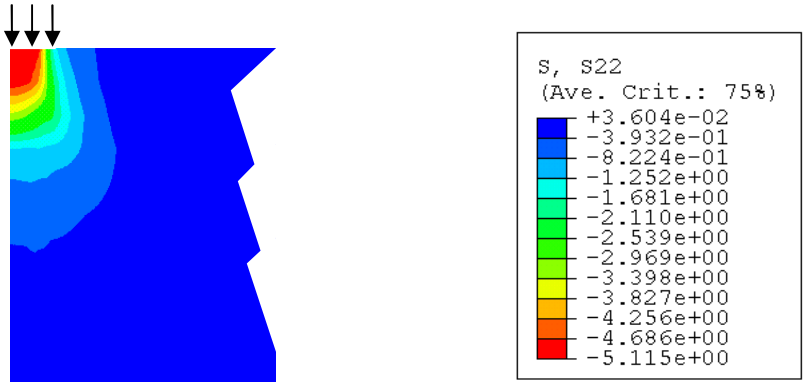

Figure 27b. Force attenuation for small load

For varying values of *r*, the maximum pressure which is present at the base of the pad has been recorded. The data is presented in Figure 28, with the detectable pressure represented as a percentage of the applied pressure.

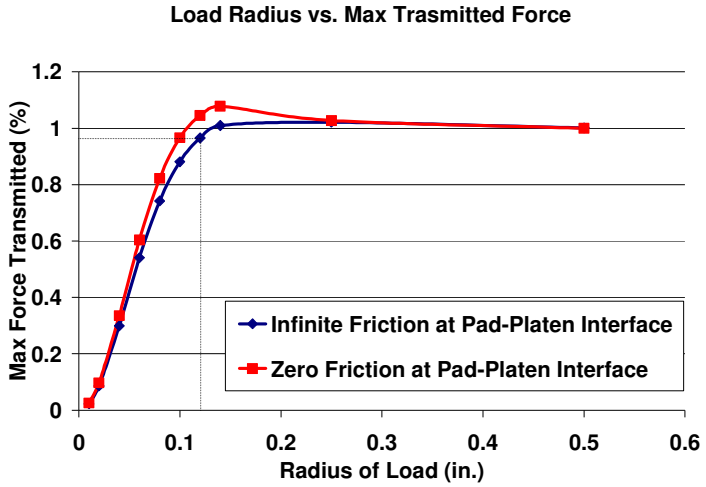

Figure 28. Force attenuation vs. load size (single pad layer)

As Figure 28 indicates, at a radius below 0.12" there is a dramatic decrease in the maximum pressure that is transmitted to the base of the pad. Thus, designing the sensor layout to sense loads with a radius smaller than 0.12" will yield diminishing returns. As further evidence of this, an additional simulation was performed in which a three-dimensional pad model was created, and regions of pressure were applied in a

"checkerboard-type" pattern. The surface loading conditions applied to the models are shown in Figure 29a/b, where red zones reflect no load, and blue reflects 5psi. In this case, each 5 psi and 0 psi region can be considered an independent "feature". Using this definition, the two figures contain 25 and 100 features/in^2, respectively. The pressure profiles at the bottom of the pad is presented for these two simulations in Figure 30a and b. Although both profiles differ from the pressures applied to the top of the pad, the profile beneath the 25 features/in^2 case still exhibits the checkerboard pattern in the pressure, while the 100 features/in^2 case appears to be nearly uniform. This simulation illustrates that when dealing with small loads it is not possible to infer the applied pressure from the sub-pad pressure profile.

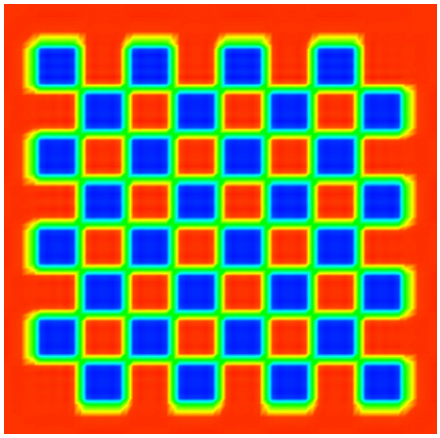

Figure 29 a. surface loading with 25 features/in^2

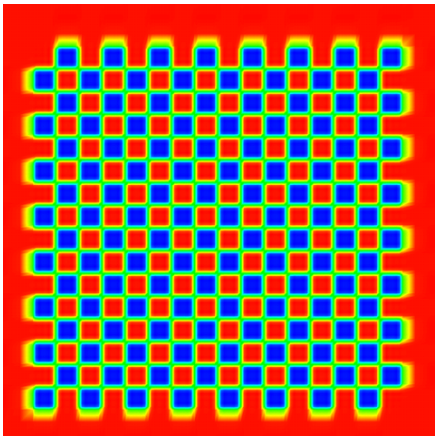

b. surface loading with 100 features/in^2

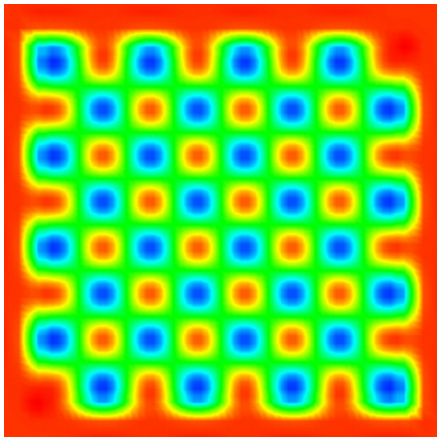

Figure 30 a. base profile with 25 features/in^2

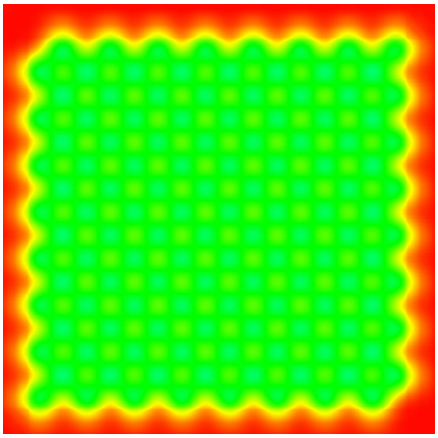

b. base profile with 100 features/in^2

As a more practical example of how force attenuation might negatively influence the recorded data, contact between a pad and a rigid wafer was simulated. Figure 31 presents the pressure profile present both at the pad/wafer interface, as well as at the base of the pad. As expected, there is a sharp rise in the pressure towards the edge of the wafer. However, the pressure at the base of the pad does not reflect these edge effects due to the force attenuation through the pad.

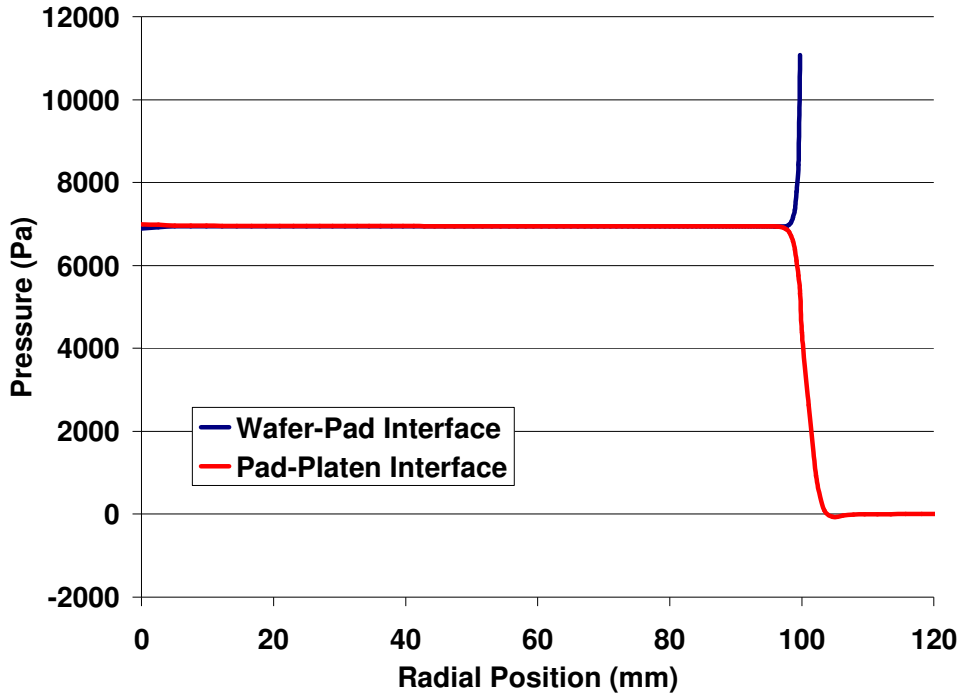

Figure 31. Simulated contact with rigid wafer

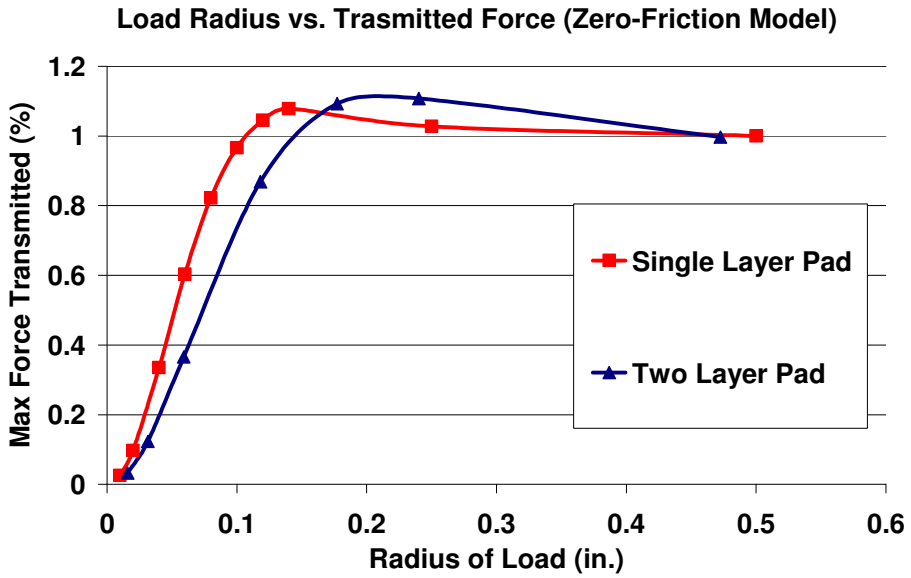

Figure 32. Force attenuation (two-layer model)

It is worth noting that the maximum pressure referenced in the preceding figures occurs at the very center of the load only, and diminishes with increased distance, as shown in Figure 32. Because a sensor placed at the base of the pad will have some non-trival area, this maximum pressure value will not be detected, rather the pressure present over the entire sensor will be averaged.

5.3. Mold sensor design and applications for Continuous-Casting: Many problems in the continuous casting process arise during initial solidification at the meniscus in the mold, including defects in the final cast product as well as cracks in the mold surface due to thermal stress. These problems dictate many aspects of steel quality and productivity.

Although the mold hot face is an ideal location to monitor, it presents a very hostile environment, with copper mold surface temperature ranges from 200 to 400°C, with instantaneous spikes that might reach even hotter during a mold level fluctuation. In current industrial practice, a large number of thermocouples are used in one continuous casting mold, destructively inserted into mold through channels drilled in copper mold, far from the hot face due to safety considerations. This limits their usefulness, as their response time is too slow to capture the rapid events that occur at the meniscus due to the dampening of the temperature signal caused by the thick copper mold between the solidifying steel and the thermocouple. Sticker breakout detection systems, installed in almost every caster worldwide, use thermocouple signals interpreted by control systems to take corrective action, but are limited by inadequate sensor technology and insufficient understanding of how to interpret the signals.

Work at the University of Illinois aims to implement sensors near the hotface of a continuous-casting mold used at the steel plant. The new sensors are being designed to measure heat flux and temperature within 1 mm of the meniscus to more accurately predict level fluctuations and quality problems, as well as providing additional insights into the casting process. Improved versions of the sensor strip design and manufacturing process are being developed through collaborations between the University of Illinois, where the sensor design, modeling, testing, evaluation, and implementation is being coordinated, the University of Wisconsin-Madison, where the sensor strip will be fabricated, a commercial mold manufacturer, where the strip will be attached to a commercial mold, and a commercial steel company, where the mold and sensor will be tested in service. In sum, this project aims to develop and validate a new type of in-mold sensor for use in the commercial continuous casting of steel. The aim is 1) to revolutionize online thermal monitoring of industrial continuous casting molds and 2) to create a new research tool to investigate meniscus behavior so that defect formation can be better understood.

This project has involved experimental investigation of 1) the attachment of glass fiber and nickel-based sensors onto the copper mold surface, and 2) ability to embed the sensors into the mold coating during the eletro-plating process, and computational modeling investigations of 1) heat-transfer consequences of imperfect plating to determine standards for success, and 2) mechanisms of initial solidification including heat extraction during oscillation mark formation, in order to extract useful information from the signals produced by the finished sensors in the future.

5.3.1. Experimental Studies: sensor strip attachment and electroplating embedding: A design for the sensor and its installation into a continuous casting mold is proposed in Figure 33. The sensor pad containing the wire junction points will protrude out of the top of the copper mold and nickel plating, thereby making wire connections possible after plating. These wires will be run a short distance to a wireless transmitter which will transmit the signal to the control-room operator display or other computer. A wireless thermocouple system that is compatible with the sensor was obtained from MicroStrain. The system supports simultaneous data transmission from multiple sensors, theoretically allowing thousands of sensors to be installed into a mold.

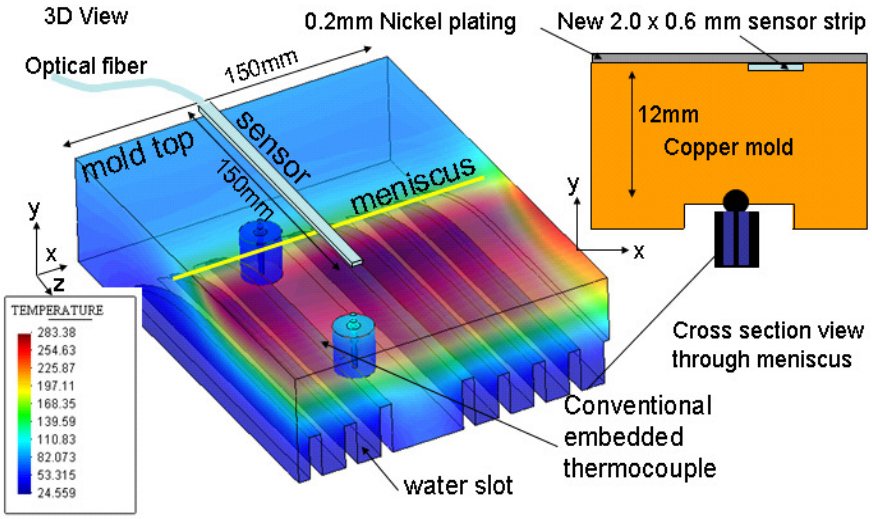

Figure 33: Sensor strip bonded into narrow face of casting mold

Before any research can be carried out to understand the behavior of embedded sensors, it is imperative that a robust method be developed to embed sensors in manufacturing tooling. Therefore, there is an absolute need to refine the embedding process through plating studies, as the sensor strip will be attached to the copper mold via the electroplating process used to apply the nickel coating layer. Any attachment method must provide a secure bond between the sensor strip and the copper mold face, have no air gaps, survive the acid pretreatment steps, and allow the sensor strip to be plated successfully before the copper mold can be put into service. It is possible to attempt to plate the sensor strip, which is fabricated encapsulated by nickel, by placing it on the copper mold face and submerging the mold face into the plating tank of the mold manufacturer. Two different trials spanning a range of aspect ratios were performed to evaluate the plating ability to attach a nickel strip to a copper substrate via commercial nickel electroplating. It was proposed to repeat the initial plating study with aspect ratios down to 0.33 in order to observe complete filling. The analysis of this plating study is currently being conducted.

Another possible method is to attach the sensor to the mold face before the plating operation is carried out. An electrically and thermally conductive silver paste (k=109 W/m-K) used in adhesive and coating applications to 1200°F has also been considered due to the ease at which trials can be conducted. Ultrasonic welding and diffusion bonding have been proposed as possible solutions. An ultrasonic welding equipment manufacturer agreed to perform an ultrasonic welding experiment to determine the feasibility of attaching a nickel strip to a copper substrate. Thus far ultrasonic welding has not proven itself an acceptable solution to the sensor attachment problem.

Fiber optic sensors are being pursued as an alternative to sensor strips. As with sensor strips, embedded fiber optic sensors have the advantage of real-time monitoring at critical locations as well as immunity to electromagnetic interference and resistance to hostile environments. Initial attempts to embed optical fibers have been met with success. Further trials with fully functioning fiber optic sensors have been planned.

Once it has been shown that a sensor can be successfully plated within the nickel layer over a copper mold, the bond between the sensor, nickel plating layer, and copper substrate can be tested. An initial check of the sensor will be performed by the mold manufacturer by immersing the copper substrate in water and applying a flame to the nickel plating layer. Any deterioration of the plating layer such as spalling or cracking will indicate a failed plating attempt.

Findings include:

- The wireless system was tested in the presence of an electromagnetic field at a commercial steel company and was shown to maintain communication between the thermocouple node and base station transceiver.
- During the initial plating study, nickel adhered well to the top, bottom, and sides of the nickel strip, as well as the copper substrate, as depicted in Figure 34.
- Often, when electroplating onto a thin strip suspended a small distance from the substrate, a void commonly forms in the gap, due to the starvation of nickel atoms when two sections of growing grains impinge just past the edge of the nickel strip. This also causes the void width to extend wider than the strip width, seen as seams at the edge of the void.
- The rate of plating is greatest in areas where sharp corners exist, due to higher current density.
- More plating reaches under the nickel strip as the sensor width decreases and/or gap thickness increases. More specifically, more plating reaches under the nickel strip as the aspect ratio, defined as the strip width over gap thickness, decreases.
- Complete filling under the nickel strip is predicted to occur when the aspect ratio is less than or equal to one.
- A sensor strip can be attached to a copper substrate via conductive silver paste and successfully plated over without any air gaps. However, the time and skill involved in this process is considerable.
- According to the ultrasonic welding equipment manufacturer, past experiences have indicated that ultrasonic welding near, around, or on top of sensors has lead to irreversible damage.
- Although the ultrasonic welding equipment is able to attach the two dissimilar metals, the machining pattern caused by the weld horn is unavoidable.
- Due to their non-conductivity and geometry, fiber optic sensors can be plated over without an air gap developing (Figure 35). This gives excellent potential for a working sensor!

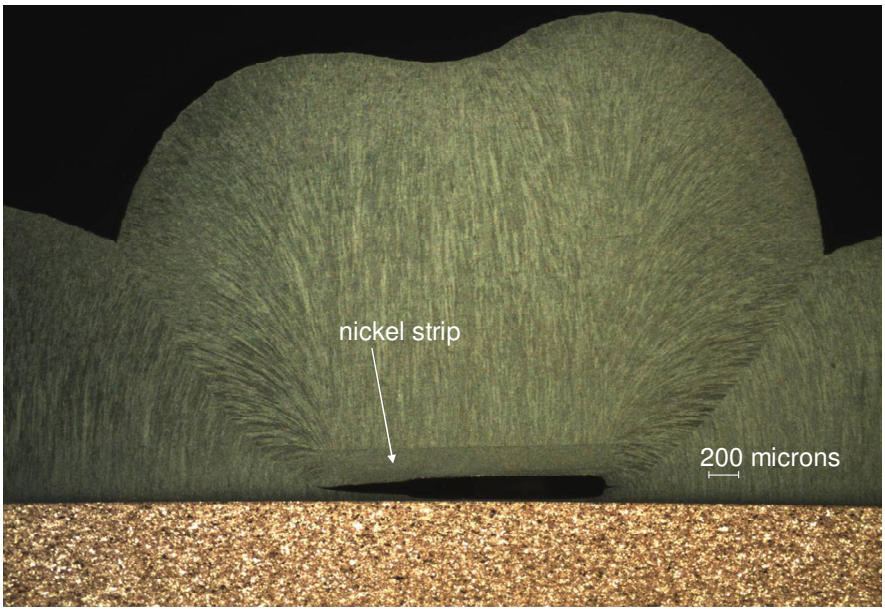

Figure 34: Nickel plated copper substrate with nickel strip, showing detrimental air gap that forms with this methodology and geometry.

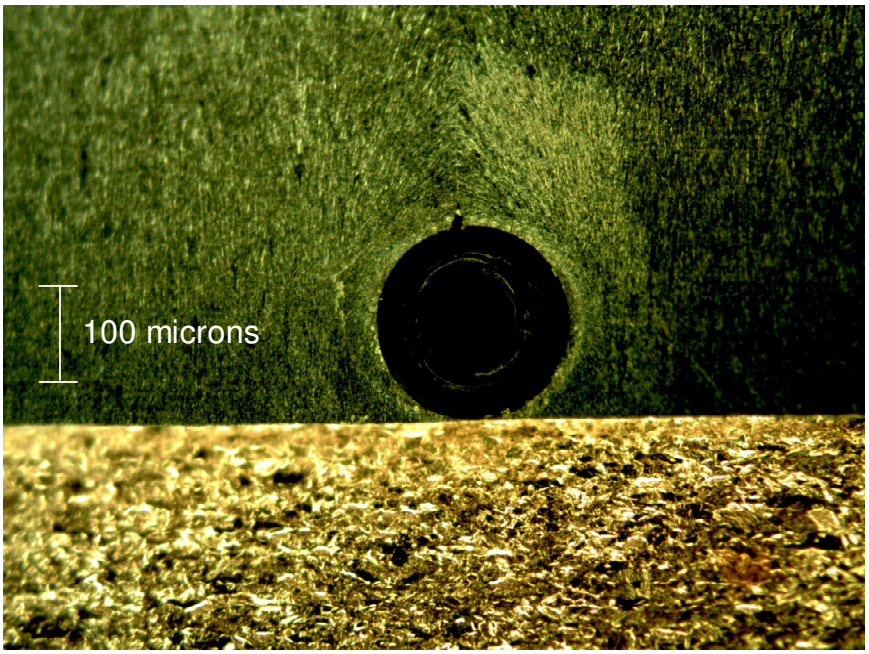

Figure 35: Cylindrical optical fiber sucessfully embedded in nickel plating layer near copper substrate, showing very promising contact with continuous embedding

5.3.2. Modeling Studies: Consequences of Gap Formation and Initial Solidification Phenomena: An incorrect plating procedure can result in an air gap forming between the sensor strip and copper substrate. In service an air gap present in the continuous casting mold can limit heat transfer and cause a localized high temperature region near the sensor. Such a temperature increase can contribute to plating layer failure or lead to the sensor spalling off. Computational models have been utilized to quantify this behavior. This is needed in order to evaluate the maximum size of gap that would still allow performance of the sensor.

Findings include:

- An air gap in the nickel plating layer can cause stress to increase by 19%.
- A wider gap makes it more difficult for heat to conduct around the gap, increasing the

temperature at the hotface: doubling the width of the air gap increases the hotface temperature by 65°C, while doubling the thickness of the air gap increases the hotface temperature by only 5°C.

5.3.3. Modeling Studies: Signal Interpretation: Sensor signals obtained online at the commercial caster was correlated with defects in cast steel found by evaluation of the cast product. This work will have the most commercial impact. Efforts have been made to identify characteristic signals or "signatures" of the formation of particular individual defects. This advances the technology towards the ultimate commercialization of an "expert mold". Improving this important process even slightly has a huge potential impact in energy savings, yield savings, steel quality, and efficiency improvement, because this particular process is used to produce several hundred million tonnes of steel every year.

Based on this work, a detailed mechanism of initial solidification has been developed and verified: oscillation marks and hooks, which comprise the initial solidification structure, form due to meniscus freezing and overflow. This brings heat to the meniscus in a characteristic periodic heat flux, which is usually increasing during the negative strip time. A detailed transient computational model of meniscus motion and heat transfer including the effects of surface tension, interfacial slag consumption, and molten steel flow has revealed the fundamentals of this behavior and a detailed mechanism for the phenomena. This is summarized in Figure 36 and detailed in 4 publications which acknowledge this NSF grant [17-20].

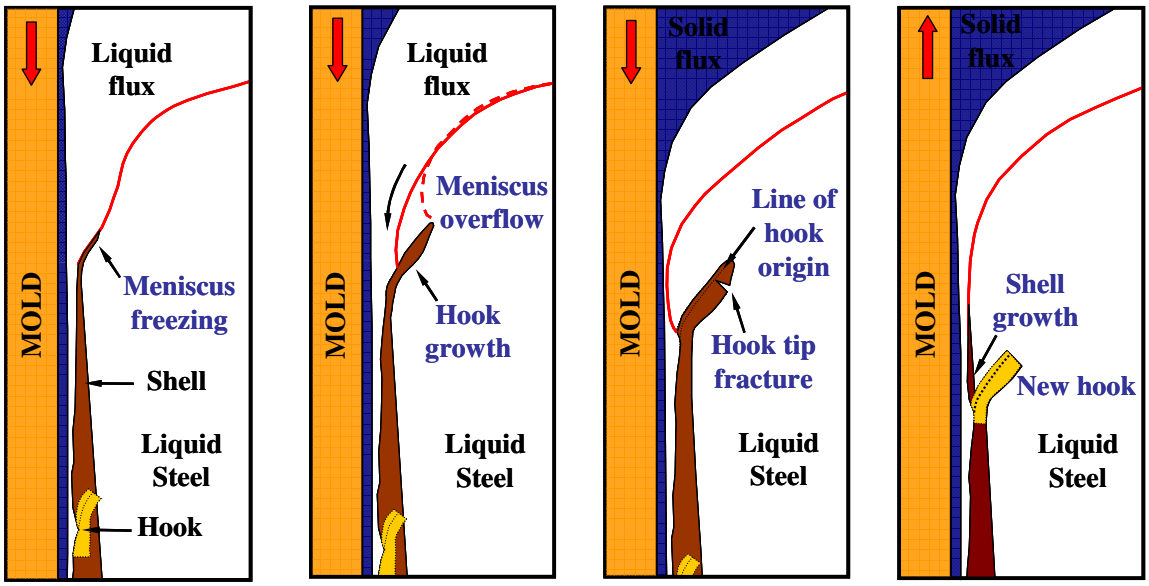

Figure 36 - Schematics illustrating formation of curved hook in an ultra-low carbon steel slab by meniscus solidification and subsequent liquid steel overflow. Oscillation marks (OM) are formed by normal steel shell growth after overflow. Their formation generates great changes in mold wall temperature during each cycle locally near the meniscus.

6. Conclusion: Integrated microphotonics have unprecedented potential for sensor enhancements for manufacturing applications. These micron-sized photonic sensors could allow critical thermo-mechanical phenomena in manufacturing processes to be monitored, while offering immunity to electromagnetic interference, resistance to hostile environments, multiplexing capabilities, and extremely high rates of data collection. Recent advances in photonic device microfabrication have made it possible to construct very small microring resonators in a variety of materials. This paper presents our research progress on integrated subwavelength photonic sensors that offers exciting new opportunities for fundamental understanding and better control of manufacturing processes.

For fundamental study, microring resonators have been microfabricated on-chip with silicon-on-insulator wafer substrates. The fabricated optical resonators offer *Q*s on the order of 20,000, enabling significantly improved temporal sensing and detection of high-frequency strain variation. The small-sized resonators also permit spatial resolution at least two orders of magnitude better than conventional fiber Bragg sensors.

A new approach to fabricate metal embedded photonic structures based on standard microfabrication techniques and electroplating was developed, in which a batch of device fabricated on a silicon wafer were directly transferred and embedded into electroplated metals. Various thin film photonic materials were studied for embedded microphotonic sensors. Thin film photonic layers of alumina and silicon nitride/alumina/ nickel were annealed at 600 ^{o}C for 10 hours and no apparent interdiffusion and delamination between thin films were found. Effect of process parameters on refractive index of silicon nitride/silicon oxynitride films was studied.

Chemical Mechanical Polishing—a key process in semiconductor manufacturing—could benefit significantly from in-situ pressure and shear feedback. Issues on design and implementation of micro sensors for Chemical Mechanical Planarization (CMP) were studied and a grafting process was designed to embed micro sensors into polishing pads. This project evaluated the sensor designed for placement beneath the CMP pad. Various challenges arise from the fact that the sensor is to be installed on a rotating surface. A wireless data-acquisition-system has been developed to overcome this complication, and is also presented in the paper.

A design for the sensor and its installation into a continuous casting mold was also developed. A key feature of this design is that the sensor will monitor temperature very near to the hotface of the steel at the meniscus, which is the most crucial part of the process. Improved versions of the sensor-strip design and manufacturing process was developed through collaborations. Based on this work, a detailed mechanism of initial solidification has been developed and verified: oscillation marks and hooks, which comprise the initial solidification structure, form due to meniscus freezing and overflow. A detailed transient computational model of meniscus motion and heat transfer including the effects of surface tension, interfacial slag consumption, and molten steel flow has revealed the fundamentals of this behavior and a detailed mechanism for the phenomena.

7. References

[1] S.T. Chu et al., “An 8-channel add/drop filter using vertically coupled microring resonators over a cross-grid,” Photonics Technol. Lett., 11, 691-693, 1999.

[2] P. Rabiei et al., “Polymer micro-ring filters and modulators,” J. of Lightwave Technol., 20, 1968-1975, 2002.

[3] B. E. Little et al., “Ultra-compact Si-SiO2 microring resonator optical channel dropping filters,” Photonics Technol. Lett., 10, 549-551, 1998.

[4] D. J. W. Klunder, “Vertically and laterally waveguide-coupled cylindrical microresonators in Si3N4 on SiO2 technology,” Appl. Phys. B 73, 603-608, 2001

[5] A. Melloni et al., “Ring-resonator filters in silicon oxynitride technology for dense wavelength-division multiplexing systems,” Opt. Lett., 28, 1567-1569, 2003.

[6] D. Rafizadeh,”Waveguide-coupled AlGaAs/GaAs microcavity ring and disk resonators with high finesse and 21.6 nm free spectral range,” Opt. Lett., 22, 1244-1246, 1997

[7] T. Baehr-Jones, M. Hochberg, C. Walker, and A. Scherer, “High-Q ring resonators in thin silicon-on-insulator,” Appl. Phys. Lett. 85, 3346 – 3347, 2004.

[8] X.C. Li, A. Golnas, and F. Prinz, “Shape Deposition Manufacturing of Smart Metallic Structures with Embedded Sensors”, Proceedings of SPIE - The International Society for Optical Engineering, v.3986, 2000, pp.160-171.

[9] X.C. Li and F. Prinz, "Metal Embedded Fiber Optic Sensors for Layered Manufacturing Process Monitoring", Journal of Manufacturing Science and Engineering, Volume 125, Issue 3, 2003, pp. 577-585.

[10] X. Li, J. Johnsen, J. Groza, and F. Prinz, “Processing and Microstructures of Fiber Bragg Grating Sensors Embedded in Stainless Steel”, Metallurgical and Materials Transactions, vol.33A, September 2002, p.3019.

[11] X. C. Li, F. Prinz, and J. Seim,"Thermal Behavior of Metal Embedded Fiber Bragg Grating Sensor", Journal of Smart Materials and Structures, no.10, 2001, pp.575-579.

[12] X. Li and F. Prinz, “Embedded Fiber Bragg Grating Sensors in Polymer Structures Fabricated by Layered Manufacturing”, Journal of Manufacturing Processes, vol. 5 No.1, 2003, pp. 78-86.

[13] B. Halg, “On a Nonvolatile Memory Cell Based on Micro-Electro-Mechanics”, Electro Mechanical Systems Workshop, Napa Valley, California, 172-176, 1990.

[14] DeJule, R., “CMP Challenges Below a Quarter Micron,” Semiconductor International, pp. 54-60 (Nov. 1997)

[15] Feeney, P., et al,”Innovation in Traditional CMP Applications,” Proc. CMP-MIC Conference, Fremont, CA, 2005, pp. 542-546

[16] B.G. Thomas, "Continuous Casting," in The Encyclopedia of Materials: Science and Technology, Vol. 2, K.H. J. Buschow, R. Cahn,

M. Flemings, B. Ilschner, E. J. Kramer, S. Mahajan and D._Apelian_subject_ed., eds., Elsevier Science Ltd., Oxford, UK., 2001, 1595-1599

[17] Sengupta, J., B.G. Thomas, H.J. Shin, G.G. Lee, and S.H. Kim, "Mechanism of Hook Formation during Continuous Casting of Ultra-low Carbon Steel Slabs", Metallurgical and Materials Transactions A, Vol. 37A, No. 5, (May), 2006, pp. 1597-1611..

[18] Ojeda, C., J. Sengupta, B.G. Thomas, J. Barco, J.L. Arana, "Mathematical Modeling of Thermal-Fluid Flow in the Meniscus Region During an Oscillation Cycle", AISTech 2006 Steelmaking Conference Proc., (May 1-4, Cleveland, OH), AIST, Warrendale, PA, Vol. 1, 2006, pp. 1017-1028.

[19] Sengupta, J., et al., *Mechanism of Hook Formation in Ultra-low Carbon Steels based on Microscopy Analysis and Thermal-stress Modeling*, in *AISTech 2006 Steelmaking Conference Proc.* 2006, AIST, Warrendale, PA: May 1-4, Cleveland, OH. p. 903-914.

[20] Thomas, B.G., J. Sengupta, and C. Ojeda, *Mechanism of Hook and Oscillation Mark Formation In Ultra-Low Carbon Steel*, in *Second Baosteel Biennial Conference*. 2006, Baosteel, Shanghai, PRC: May 25-26, 2006, Shanghai, PRC. p. 112-117.